# TWO-YEAR OBSERVATIONS OF THE JUPITER POLAR REGIONS BY JIRAM ON BOARD JUNO

Adriani A. (1), Bracco A. (2), Grassi D. (1), Moriconi M.L. (3), Mura A. (1), Orton G. (4), Altieri F. (1), Ingersoll A. (5), Atreya S.K. (6), Lunine J.I. (7), Migliorini A. (1), Noschese R. (1), Cicchetti A. (1), Sordini R. (1), Sindoni G. (8), Plainaki C. (8), Dinelli B.M. (3), Turrini D. (1), Filacchione G. (1), Piccioni G. (1), Tosi F. (1), Bolton S.J. (9).

(1) INAF - Istituto di Astrofisica e Planetologia Spaziali, Roma, Italy
(2) Georgia Institute of Technology, Atlanta, Georgia, USA
(3) CNR - Istituto di Scienze dell'Atmosfera e del Clima, Bologna and Roma, Italy
(4) Jet Propulsion Laboratory, California Institute of Technology, Pasadena, California, USA
(5) California Institute of Technology, Pasadena, California, USA
(6) University of Michigan, Ann Arbor, Michigan, USA
(7) Cornell University, Ithaca, New York, USA
(8) Agenzia Spaziale Italiana, Roma, Italy
(9) Southwest Research Institute, San Antonio, Texas, USA

Corresponding author: Alberto Adriani (alberto.adriani@inaf.it)

## Key Points:

- **The** Jupiter's polar cyclonic structures, both in the North and in the South Poles**, did not change much in two years of observations from February 2017 to February 2019.**
- **This study reports** abundances of atmospheric minor constituents **-** water, ammonia, phosphine and germane **- measured** in the **hottest spots of the** polar regions **with higher values registered in the south.**
- **The** analysis of the polar **structures' dynamics shows similarities to the** Earth oceanic cyclones.

## Abstract

We observed the evolution of Jupiter's polar cyclonic structures over two years between February 2017 and February 2019, using polar observations by the Jovian InfraRed Auroral Mapper, JIRAM, on the Juno mission. Images and spectra were collected by the instrument in the 5-μm wavelength range. The images were used to monitor the development of the cyclonic and anticyclonic structures at latitudes higher than 80° both in the northern and the southern hemispheres. **Spectroscopic** measurements **were** then **used to monitor** the abundances of minor atmospheric constituents water vapor, ammonia, phosphine and germane in the polar regions, where the atmospheric optical depth is less than 1. Finally, **we performed** a comparative analysis with oceanic cyclones on Earth in **an** attempt to explain the spectral characteristics of the cyclonic structures we observe in Jupiter's polar atmosphere.

## Plain Language Summary

The Jovian InfraRed Auroral Mapper (JIRAM) is **an instrument** on-board the Juno NASA spacecraft. It **encloses of** an infrared camera, for mapping both **Jupiter's auroras** and **atmosphere,** and a spectrometer.

In February 2017, the complex cyclonic structures that characterize the Jupiter's polar atmospheres were discovered. **Here, we** report the evolution **of** those cyclonic structures during the 2 years following the discovery**. For the purpose, we use** infrared maps built by the **JIRAM** camera images collected at wavelengths around 5 μm.
**The** cyclones **have thick clouds which** obstruct most of the view of the deeper atmosphere. However, some areas, near the cyclones, are **only** covered by **thin** clouds **allowing** the spectrometer **to** see below **deeper in** the **atmosphere**. In those areas, **the instrument was** able **to catch** spectral **signatures that permitted to estimate** abundances of water vapor, ammonia, phosphine and germane**. Those gases** are minor but **significant constituents** of the atmosphere.
Finally, the dynamics of the Jupiter's polar atmosphere **are** not well understood and **are still** under study. Here, to give indications **about** the possible mechanisms that governs the polar dynamics, we attempted a comparative analysis with some Earth oceanic cyclones that show similarities with the Jupiter ones.

**Keywords:** Jupiter, Planetary Atmosphere, Polar Regions, Composition, Mesospheric Dynamics

## 1. Introduction

The Juno mission entered into Jupiter orbit in July, 2016 (Bolton et al. 2017). The Jovian InfraRed Auroral Mapper, JIRAM, is part of the payload of the spacecraft (Adriani et al. 2017). **Key goals** of this instrument **are** to collect both ~5-μm imaging (M band filter: 4.5 to 5 μm) and spectral observations in the 2-5 μm range with a spectral resolution of about 15 nm to study Jupiter's atmosphere. **The methane transparency window around 5 μm is a region dominated by the atmospheric thermal emission. However, the thermal emission is modulated by the presence of the clouds and, then, the depth of the infrared sounding depends on the cloud thickness. In absence of clouds and for small optical thickness the infrared sounding at wavelengths around 5 μm can reach depths of 4-5 bar. The imager focal plane is divided in two areas by the presence of two optical filters: one in band L dedicated to auroral mapping and the other in band M for atmospheric observations. The auroral signal is much less intense than atmospheric thermal emission, then the imager has to use different integration times in according to the target to observe. This fact means that the two observations are in competition and cannot operated simultaneously.** The imager and the spectrometer have a spatial resolution of 250 μrad and are operated simultaneously.
The great advantage of Juno's instruments, compared to all the others that have observed Jupiter for years from Earth and from other space missions, is **that Juno is in a polar orbit, allowing an unprecedented view of t**he planet's poles.

On February 2nd 2017, during the fourth fly-by, JIRAM had the opportunity to observe the polar atmosphere of Jupiter for the first time (Adriani et al. 2018). Those observations, together with those of the visible JunoCam imager **(Hansen et al, 2014),** allowed us to survey for the first time the dynamical structure of the polar atmosphere of the planet. The North Pole exhibits a polar cyclone **(or NPC)** surrounded by eight circumpolar cyclones (or CPCs) while the South Pole is characterized by five cyclones surrounding a polar cyclone. The CPCs have approximately the same size as their respective central polar cyclones; the southern cyclones are larger than the northern ones.

JIRAM's observation of Jupiter's poles has continued since February 2017 during fly-bys with favorable spacecraft attitudes and when auroral observations by JIRAM were not scheduled. For the sake of simplicity we identify **Juno** orbits with the label PJ (PeriJove) followed by the orbit number. The spacecraft attitude was generally not favorable to the JIRAM observations during orbits when the mission optimized the gravitational mapping of Jupiter (GRAV orbits). Additionally, the

instrument can only observe targets that are within ±3° **of** the plane orthogonal to the spacecraft spin axis. A limited number of orbits have been dedicated to remote sensing instrumentation on board of Juno. During orbits when the MicroWave Radiometer (MWR) was the prime instrument, JIRAM could observe the planet during the approach and reasonably cover the North Pole. Orbit 9 (PJ9) was the last **one in which** JIRAM had a reasonably good coverage of the Pole. On the other hand, the South Pole could be observed almost during every perijove pass with good coverage and spatial resolution.

Table 1 provides a summary of the observations **for which we were able to obtain good coverage of the polar regions**: four for the North Pole and ten for the South Pole. Observations with more limited coverage have been excluded from this analysis. Given that Juno maintains a polar orbit of about 53 days, that is the minimum time interval between two successive observations reported here. The spatial resolution at the 1-bar pressure level is variable and ranges from about 15 km to about 60 km, depending on the position of the spacecraft in the orbit.

| Date | Orbit # | Orbit type | Pole | Average Resolution | Images # |
|---|---|---|---|---|---|
| 02/02/2017 | 4 | MWR | North | 51 km | 9 |
| | | | South | 55 km | 11 |
| 05/19/2017 | 6 | MWR | North | 23 km | 45 |
| | | | South | 59 km | 12 |
| 09/01/2017 | 8 | GRAV | South | 47 km | 18 |
| 10/24/2017 | 9 | MWR | North | 39 km | 40 |
| | | | South | 16 km | 40 |
| 12/16/2017 | 10 | GRAV | North | 15 km | 14 |
| 02/07/2018 | 11 | GRAV | South | 44 km | 17 |
| 05/24/2018 | 13 | GRAV | South | 53 km | 12 |
| 07/16/2018 | 14 | GRAV | South | 57 km | 10 |
| 09/07/2018 | 15 | GRAV | South | 61 km | 23 |
| 12/21/2018 | 17 | GRAV | South | 49 km | 16 |
| 02/12/2019 | 18 | GRAV | South | 46 km | 14 |

Table 1. Summary of the polar observations. The average resolution reported here is calculated at 1-bar level and it is referred to the mosaics shown in Figures 1, 2 and 3. It is the result of the resampling of the single images at a homogeneous spacing. Last column shows the number of images used for composing the mosaics of Figures 1,2 and 3.

**Moreover, while tropospheric composition in hot spots and in extended regions at Jupiter's low and intermediate latitudes has been investigated by a number of authors on the basis of spacecraft and ground-based telescope data (e.g. Giles et al. 2015 and Giles et al. 2017), no study has yet covered the polar regions. However, starting from the Juno's fourth perijove (PJ4, February 2nd 2017) JIRAM has gradually acquired extensive observations over both poles. Here we calculate the tropospheric content of water, ammonia, phosphine and germane at Jupiter's polar regions from JIRAM spectral data in those areas where the atmospheric optical depth is lower than 1.**

**Finally, in order to give a contribute to the understanding of the dynamic processes that regulate the circumpolar structural of the Jupiter we attempt a parallel with oceanic cyclone observed on Earth.**

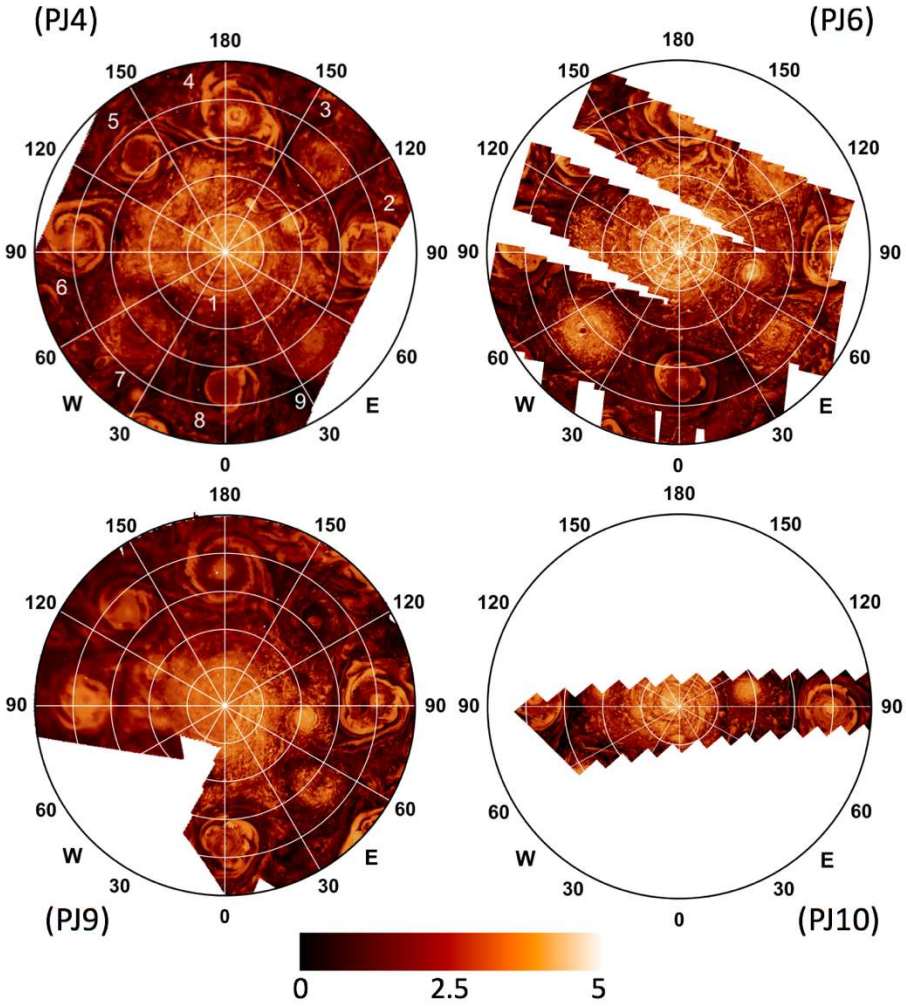


**Figure 1.** North pole during PJ4, PJ6, PJ9 and PJ10 (from top to bottom al left from right). Whitish colors indicate higher optical depth (τ), i.e. thicker clouds. Cyclone numbering: the polar cyclone is #1; the cyclone at 90E is #2; the numbering proceeds counterclockwise from #3 to #9. The color bar on the bottom indicates the value of τ.

## 2. Observations

Table 1 reports the pixel resolutions of the mosaics built by single stereographic maps based on System III longitude and planetocentric latitude coordinates and the number of images used for the relative mosaics. Mosaics are shown in Figures 1, 2 and 3: Figures 1 refers to the North Pole observations while Figures 2 and 3 refer to those at the South Pole. All the observations and the analysis reported here are at a latitude higher than 80°N and 80°S. **All the single images used in this work, as well as the plots in the mosaics of Figures 1, 2 and 3, have been corrected by the Beer's law, and the data were chosen so that the emission angle (the angle between the normal to the planet at the pixel location and the direction of the spacecraft) was always lower than 60° (except for the Northern cyclones #5 and #6 during PJ9). Then, Figures 1, 2 and 3 are plotted in term of optical depth, $\tau = \log(I_0/I)$, that is normalized to the value $I_0 = 0.65624$ Wm$^{-2}$ which is the maximum radiance measured at latitudes higher than 80° either in the north or in the**

**south. In this scheme, light colors represent thicker clouds. Namely, the figures show the polar regions cloudiness making them easier to compare to the visual camera observations of JunoCam, the camera on-board Juno. All JunoCam images, since the beginning of the mission are available on the Juno Mission website at https://www.missionjuno.swri.edu/junocam.**
**All the reported data have a geographical reference. We use NAIF-SPICE (Acton, 1996) and ENVI tools (by https://www.harrisgeospatial.com/Software-Technology/) for each geometric calibration and image processing. Ultimately, the pictures in Figures 1, 2 and 3 are compositions obtained by assembling different image sequences taken by JIRAM. They are plotted on geographic coordinates and show the maps of τ (as defined above) for the two poles. Significant differences between North and South are readily apparent from a visual comparison of Figure 1 versus Figures 2 and 3.**

In Figure 1, we present the sequence of four North Pole observations summarized in Table 1. As stated previously by Adriani et al. (2018), the dynamic structure of this pole is shaped in such a way that the cyclones surrounding the polar one are approximately located on the vertices of a ditetragonal pattern. Some of the cyclones kept their cloud patchy structures in the eight months between PJ4 and PJ9, while others showed more clearly ordered cloudy spiral configurations with small cyclones or anticyclones inside the main structure. In general, the CPCs arrangement was quite stable during this entire period, and the internal structure of the single cyclones did not change significantly– including the one visible in PJ10.

Beside the small fluctuation of the CPCs around their average position, a big anticyclone was located around 87$^{o}$N latitude. It has been present since the first JIRAM observation during PJ4 (February 2017) **and was still present during** PJ10, a period slightly longer than 10 months. In this time span, it grew slightly in size **from about 1,400 km** up to about 2,000 km in diameter, oscillating between 80$^{o}$E and 120$^{o}$E longitudes in the "channel" between the polar cyclone and the circumpolar cyclones. Its changes in position can be clearly detected in Figure 1. Unfortunately, its later evolution could not be monitored due to the poor JIRAM coverage of the North Pole that resulted from the spacecraft attitude change during the remaining part of the mission.

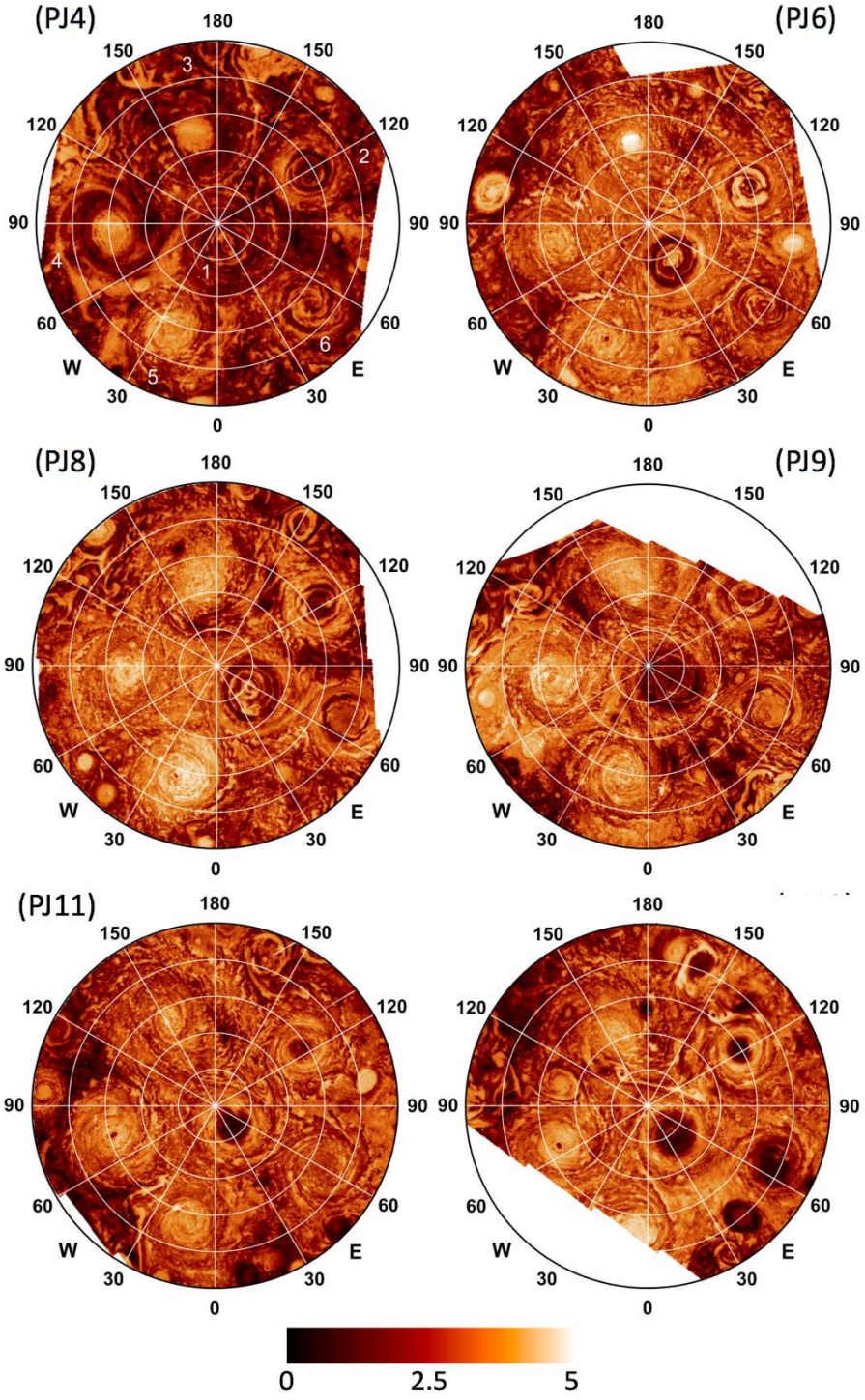


**Figure 2.** South pole from PJ4 to PJ13 (from top to bottom al left from right). Whitish colors indicate higher optical depth (τ), i.e. thicker clouds. Cyclone numbering: the polar cyclone is #1; the cyclone at the longitude of approximately 120E is #2; the numbering proceeds counterclockwise from #3 to #6. The color bar on the bottom indicates the value of τ.

In Figures 2 and 3 we present the sequence of ten South Pole observations summarized in Table 1. As already stated by Adriani et al. (2018) following the PJ4 observation in February 2017, the South Pole configuration is quite different from the northern one. The South Pole observations have continued on regular basis, and here we report about the evolution between PJ4 and PJ18. During a

time lapse of two years the pentagonal structure remained substantially unchanged, with only occasional perturbations.

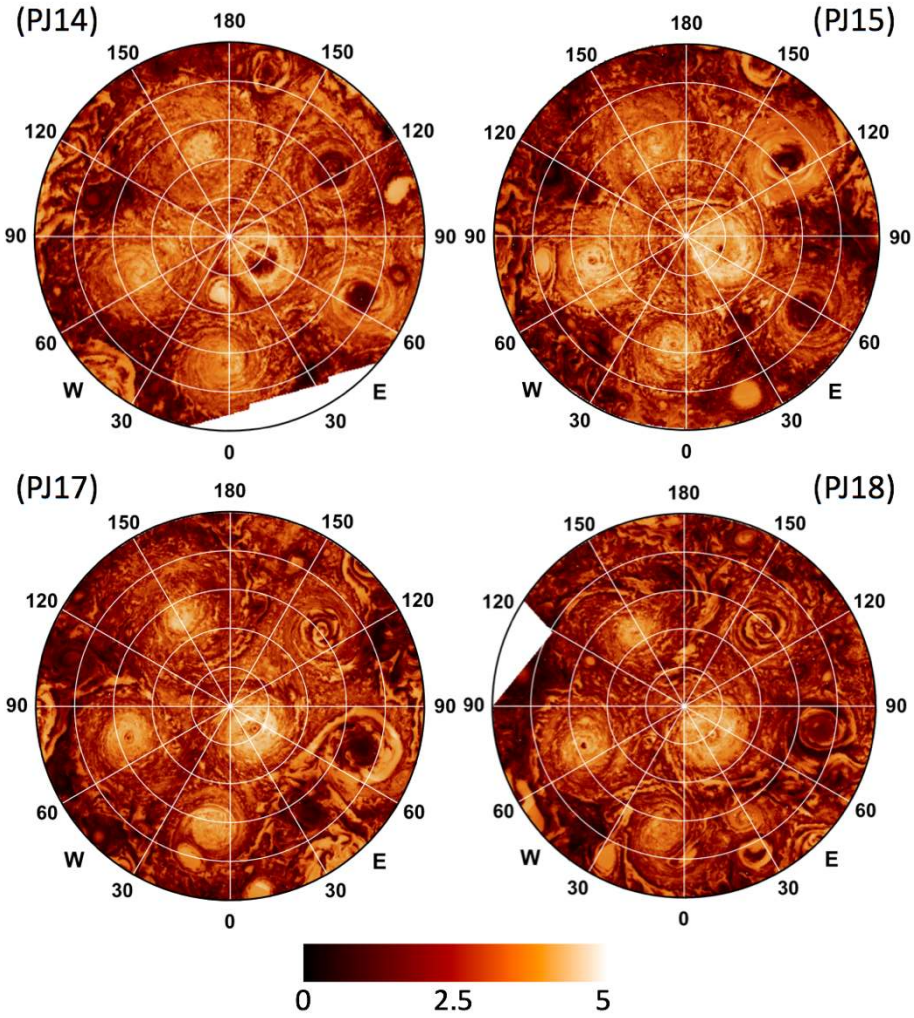


**Figure 3.** South pole during PJ14 to PJ18 (from top to bottom al left from right). Whitish colors indicate higher optical depth (τ), i.e. thicker clouds. Cyclone numbering: the polar cyclone is #1; the cyclone at the longitude of approximately 120E is #2; the numbering proceeds counterclockwise from #3 to #6. The color bar on the bottom indicates the value of τ.

As in the north, the six cyclones **slightly changed their internal structure. In particular, as it can be seen in Figures 2 and 3, the group formed by cyclones 3, 4 and 5 were more stable over the two-years period while the cyclones 1, 2 and 6 were more variable in terms of cloudiness.** Unlike the North Pole, however, no long-lasting anticyclonic structures nested within the pentagonal structure were observed at the South Pole. During the first year, anticyclones appeared episodically within the cyclonic assembly but never lasted to the following perijove. On the other hand, a few relatively large anticyclones were present in the second year of the mission, from PJ13 onward. Moreover, toward the end of the period a new feature appeared between the CPCs #5 and #6 (see Figure 4 for the identification of CPC numbers). This structure is reminiscent of a vortex dipole whose embryo was already recognizable during PJ15. During PJ18 the Southern CPCs appeared to

move to a hexagonal shape where the new-born vortex is joining the previous ones around the central cyclone.

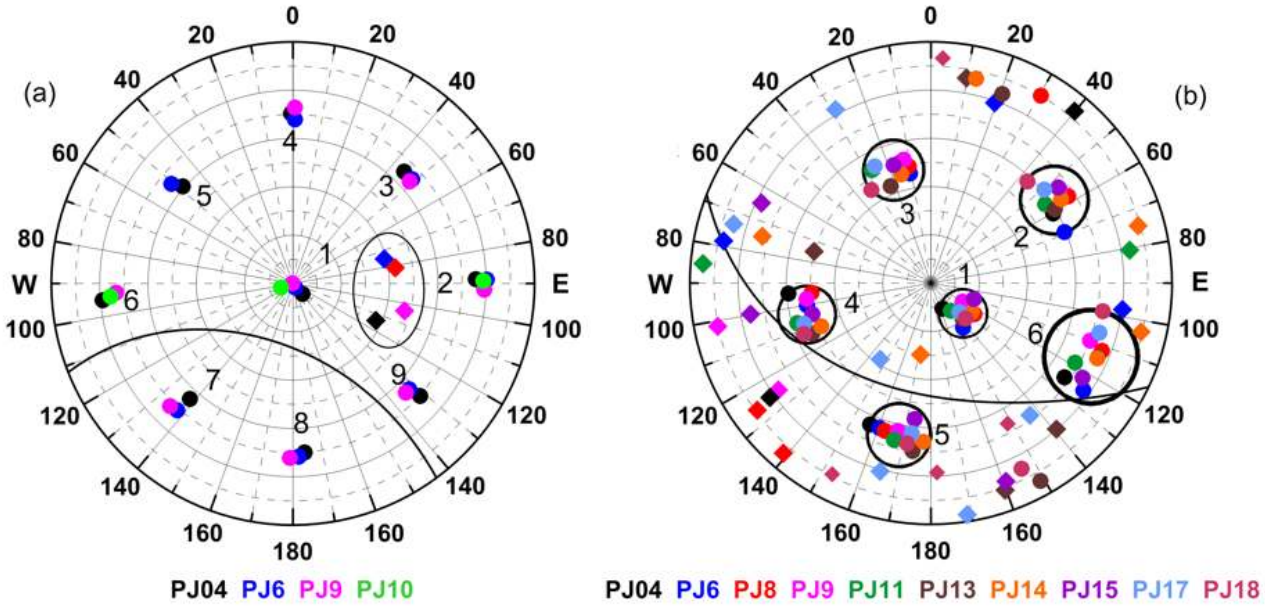


**Figure 4.** Position of the cyclone centers (dots) during the observation period for North pole [panel (a)] and South pole [panel (b)]. The colors identify the different perijoves. The black circles indicate the variation of the position of the southern cyclone centers and are centered at the average position measured in the all period of observations. The diamonds represent the position of the different anticyclones with diameters larger than 1000 km. The oval in panel (a) identify the different positions **of** the same anticyclone during the different reported perijoves.

Figure 4 illustrates the position of the cyclones and the anticyclones with diameters larger than 1000 km observed in the polar region of both hemispheres. In the almost 9 months during which we could get good coverage of the North Pole no anticyclones of sizes larger **than 1000** km were observed at latitudes higher than 80°N beside the one hovering at 87°N between the NPC and the CPCs. On the other hand, a large number of anticyclones were observed in the southern regions, particularly at longitudes between 100°E and 300°E. Most of them appeared to be connected to a cyclone in a dipole configuration. Sometimes the cyclone was one of the CPCs, as in the case of CPC#5 where the anticyclone was still present during PJ19 (not shown here). During PJ18, CPC#6 moved significantly towards lower longitudes leaving space for the intrusion of a cyclone/anticyclone dipole that could anticipate the formation of a new CPC. Other cyclones with diameters larger than 1000 km occasionally grew outside the CPCs ring, but they never appeared to last for more than a 53-day perijove pass.

**The average radiances measured in the spectral range 4.5-5.0 μm are systematically higher in the north with an average value of 0.133 $Wm^{-2}$, than in the south, where the average is 0.069 $Wm^{-2}$ [Figure 5 panel (a)]. During PJ4 the southern radiance was at its highest value of 0.1 $Wm^{-2}$ followed by an abrupt decay of about 50% during PJ6, after 106 days.**

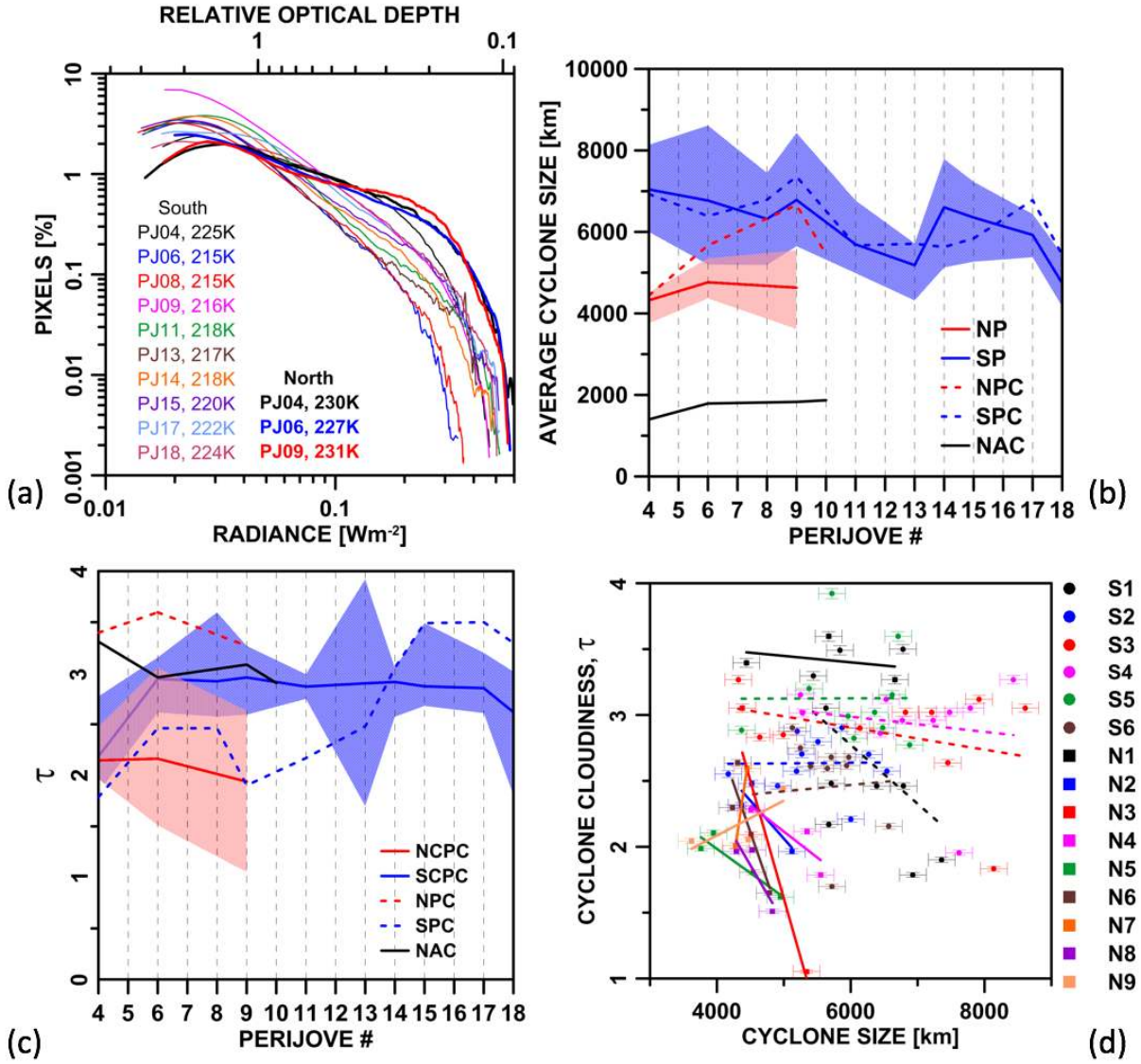


**Figure 5.** (a): Distribution of pixels radiance, the average brightness temperature at latitudes higher than 80° is given for each perijove. (b): The blue and the red curves gives the average diameter of the circumpolar cyclones for the south and the north respectively; the dashed curve account for the respective polar cyclones; the blue and the red areas show the minimum to maximum variation of the cyclones size; the black curve gives the diameter of the only larger anticyclone observed in the north; (c): optical depth of cyclones, following the color definitions for panel (b). (d): optical depth versus cyclone size; in the legend S stands for south and N for north and the numbering criterion is the same given in figures 1, 2 and 3.

A slow but progressive increase has been observed after PJ6 [see Figure 4 panel (a) for details]. Panel (a) of Figure 5 shows also the statistics of the pixels' brightness of the two poles in terms of radiance. In the legend, the corresponding average brightness temperature for each PJ and at latitudes higher than 80° N/S is also given. A direct comparison between North and South can be only done for the first year, as no north pole images in the infrared range are available after December 2017.

Some single cyclone characteristics have been investigated in order to monitor the changes that occurred in the two years of observations, from February 2017 to February 2019. Figure 5 also accounts for changes in the average diameters [panel (b)] and cloudiness [τ, in panel (c)] of the single cyclones versus time from PJ4 to PJ18. The diameters of the northern and southern cyclones are

substantially different. The average diameter of the northern cyclones is about 4,600 km. Southern cyclones, being **fewer but occupying approximately the same latitudinal extension of the northern ones are systematically greater,** their average diameter reaches approximately 6,300 km. Another difference between south and north is the relative size of the polar cyclone with respect the surrounding CPCs. While the size of the southern polar cyclone (SPC) is commensurate with the surrounding CPCs, the northern one (NPC) is significantly larger than its surrounding CPCs [see panel (b) of Figure 5]. Focusing on the time evolution of southern cyclones' sizes, we note both a general decrease and a sort of pulsation in the distribution of the dimensions: namely, sometime the cyclones are quite different from each other, but at other times their sizes are more similar. Also, from the cloudiness point of view, the NPC differs from the surrounding cyclones showing an average $\tau$ of 3.4 while its CPCs have an average value of 2.1. The opposite happens for the SPC whose cloudiness ($\tau \approx 2.2$) is systematically lower than the average cloudiness of the surrounding CPCs ($\tau \approx 2.8$). The SPC cloudiness grows significantly reaching values similar to the NPC during the last part of the time period analyzed. Finally, **in general,** the cyclones are characterized by the **tendency** to reduce **or maintain more or less the** their cloudiness when growing in size [see panel (d) of Figure 5]. **In a couple of cases we observed the opposite behavior.**

## 3. Spectral Analysis

**The spectral analysis performed here is limited to the wavelength range between 4 and 5 µm considering the only thermal emission of the planet. In fact, even if the polar regions are partially illuminated by the sun, our approximation is justified by our specific focus on the brightest areas where the scattered solar contribution in the 4-5 µm region µm is expected to be between 100 and 800 times smaller than the thermal component, as reported previously by Drossart et al. (1998).**

**Most of the polar** regions of Jupiter are affected by thick cloud coverage **but** relatively clear areas (with cloud total opacities < 1 at 5 µm) exist at some specific locations, **similarly to** the hot spots frequently observed between the Equatorial Zone and the North Equatorial Belt (Grassi et al. 2017a). Figure 6 shows the polar areas within 80°N/S latitudes where the optical depth, $\tau$, is lower than 1 at PJ4. Correspondingly, Figure 6 shows the areas where the JIRAM spectra are sensitive to the contents of ammonia, water vapor, phosphine and – in lesser degree – germane, at the approximate levels between 2 and 3 bar (Grassi et al. 2017b), well below Jupiter's tropopause level. Water and ammonia

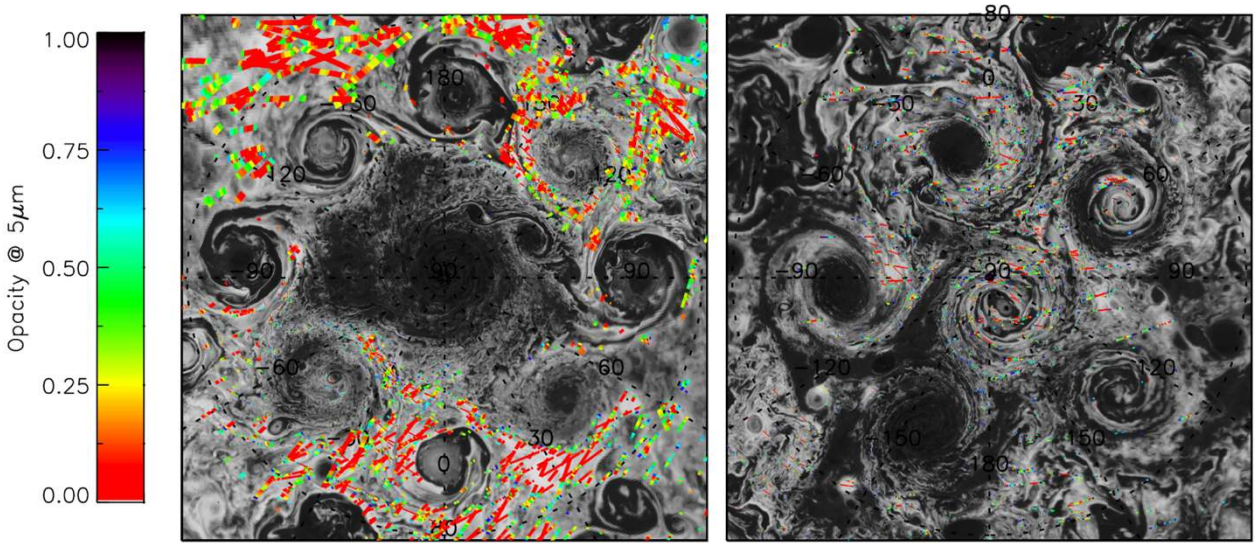


**Figure 6.** Areas where the optical depth, in the infrared wavelengths around 5 µm, is lower than 1

according to the JIRAM spectrometer data.

are condensable and involved in the cloud formation while germane and phosphine are disequilibrium species from the deep interior **and they are retrievable from JIRAM spectral data in the range 4.5-5. µm.**

**The set of parameters to be retrieved** has been defined following the scheme already proposed in Irwin et al. (1998) for hot spots. The adopted scheme aims to distinguish, where relevant, the 'deep' content of gaseous species from their mixing ratios in the upper troposphere, where depletion may occur due to condensation or photochemistry. According to that scheme, for the analysis here, we consider different free parameters: $H_2O$, $NH_3$, $PH_3$, and $GeH_4$ "deep" mixing ratios, which are all assumed to be constant with altitude; the $H_2O$ relative humidity above its condensation level and constant with altitude; and the total optical depth at 5µm of the main (putative $NH_4SH$) cloud above the water cloud. The topmost cloud layer (putatively $NH_3$) is thought to be essentially absent in hot-spot regions, while diffuse haze has been demonstrated to be transparent at 5µm.

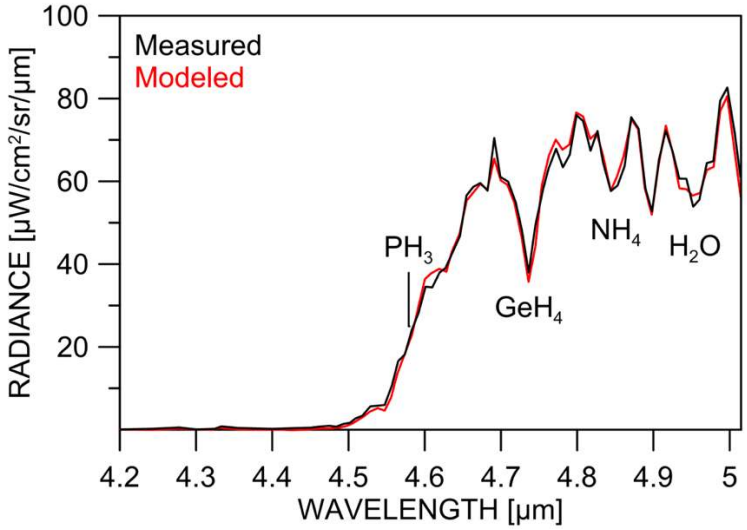


**Figure 7. Comparison between a measured and a reconstructed spectrum between 4.2 and 5 µm**

**Figure 7 displays the spectral region used for the retrieval. It also shows how the model used in the retrieval is able to reproduce the measured spectrum. Performance of the retrieval code has been quantified on the basis of test runs on large sets of simulated observations and the retrieval errors include the effects of forward-modelling errors in the radiative transfer. Notably, these errors exceed by at least a factor of 10 the instrumental Noise Equivalent Radiance, as estimated in Adriani et al. [2016]. Considering the typical nominal values of retrieval errors and assuming a mean deterioration factor 5 for all gases, we can estimate the approximate uncertainties for the retrieved contents of different gases from individual spectra as follows: $Log_{10}([H_2O]_{RH})$~0.08, [NH3]~$3.0x10^{-5}$, [PH3]~$6.0x10^{-8}$ and [GeH4]~$4.3x10^{-11}$. As water vapor is by far the most variable gas in the Jupiter atmosphere, we found therefore correct to keep the logarithm of relative humidity (i.e.: the original state vector element in our retrieval code) rather than convert it to a mixing ratio.**

**Our retrieval model uses the temperature-vs-pressure profile from Seiff et al. [1998] on the basis of the Galileo Entry Probe measurements. In order to quantify errors introduced by possible variations of the real temperature in respect the assumed value, numerical tests demonstrate that systematic increase or decrease of 5K at every fixed pressure level of our**

**atmospheric model induces a relative variation of about 2% in the retrieved contents of ammonia and phosphine, of 5% in germane and 15% of the water relative humidity value.** The analysis **presented here** was performed on PJ4 data (February 2nd, 2017**). The method was already more extensively described by** Grassi et al. (2017b) and **analysis is restricted** to spectra with low emission angle to limit retrieval uncertainties and attain higher signal.

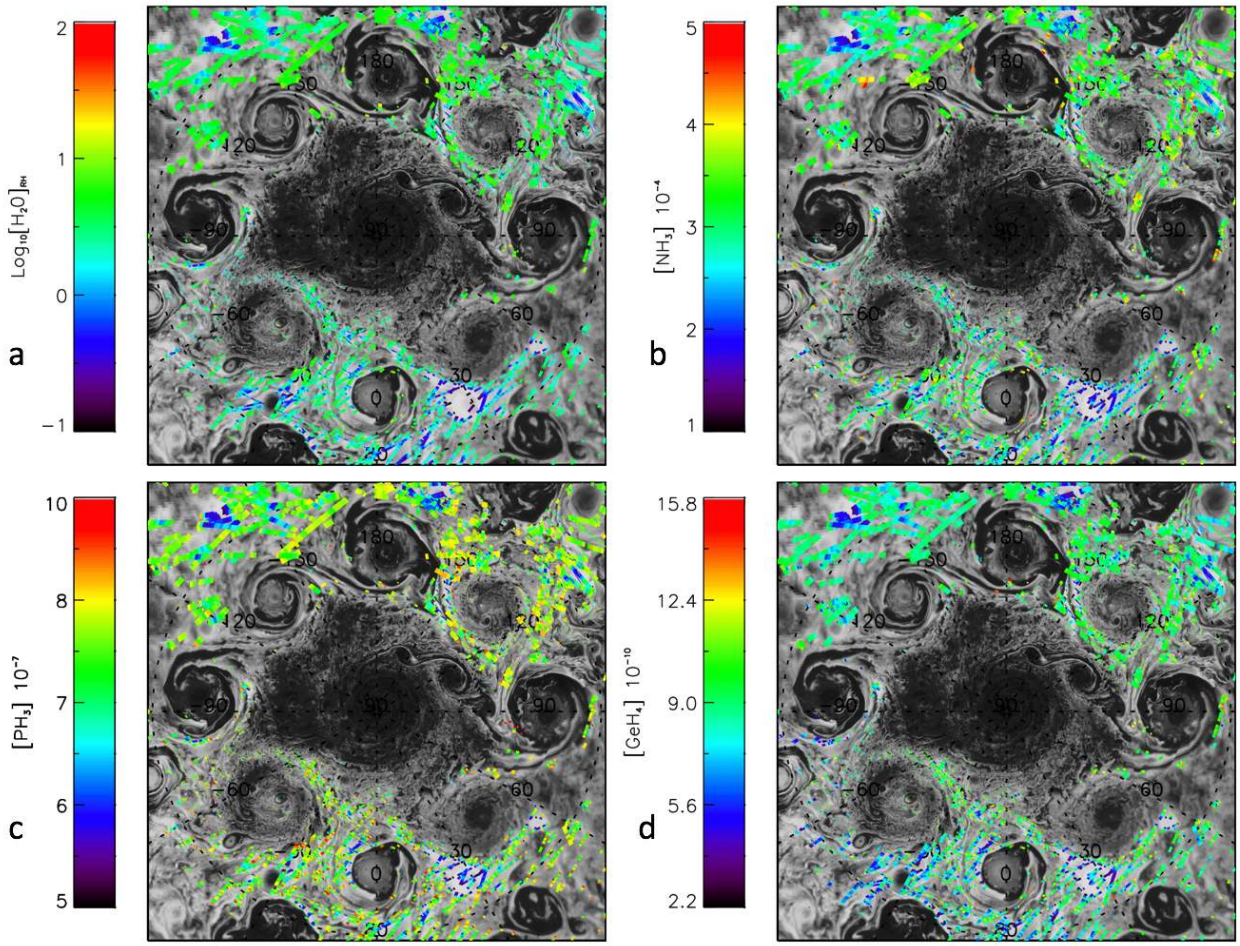


**Figure 8.** North pole maps of water relative humidity (a), ammonia (b), phosphine (c) and germane (d) concentrations.

Results of the analysis are reported in Figures 7 and 8 for the relative humidity of water vapor and the concentrations of ammonia, phosphine and germane, for the North and South Poles, respectively. The thickness of the tracks is proportional to the pixel resolution at Jupiter's 1-bar level. It is noticeable that the abundances of condensable species ($H_2O$ and $NH_3$) are more depleted over the lower-opacity regions. However, those gases appear r**el**atively enhanced over the South Pole compared to northern regions, possibly because of smaller overall opacity of cyclones in the former areas during Juno PJ4 passage. Values range between 0.3% and 10% for the water vapor relative humidity and between **100** and **500** ppm for the ammonia mixing ratio in the north (see Figure **8**), and between 0.3% and 20% for both for the water vapor relative humidity and ammonia in the south, but with an average significantly shifted toward the upper value (see Figure **9).**

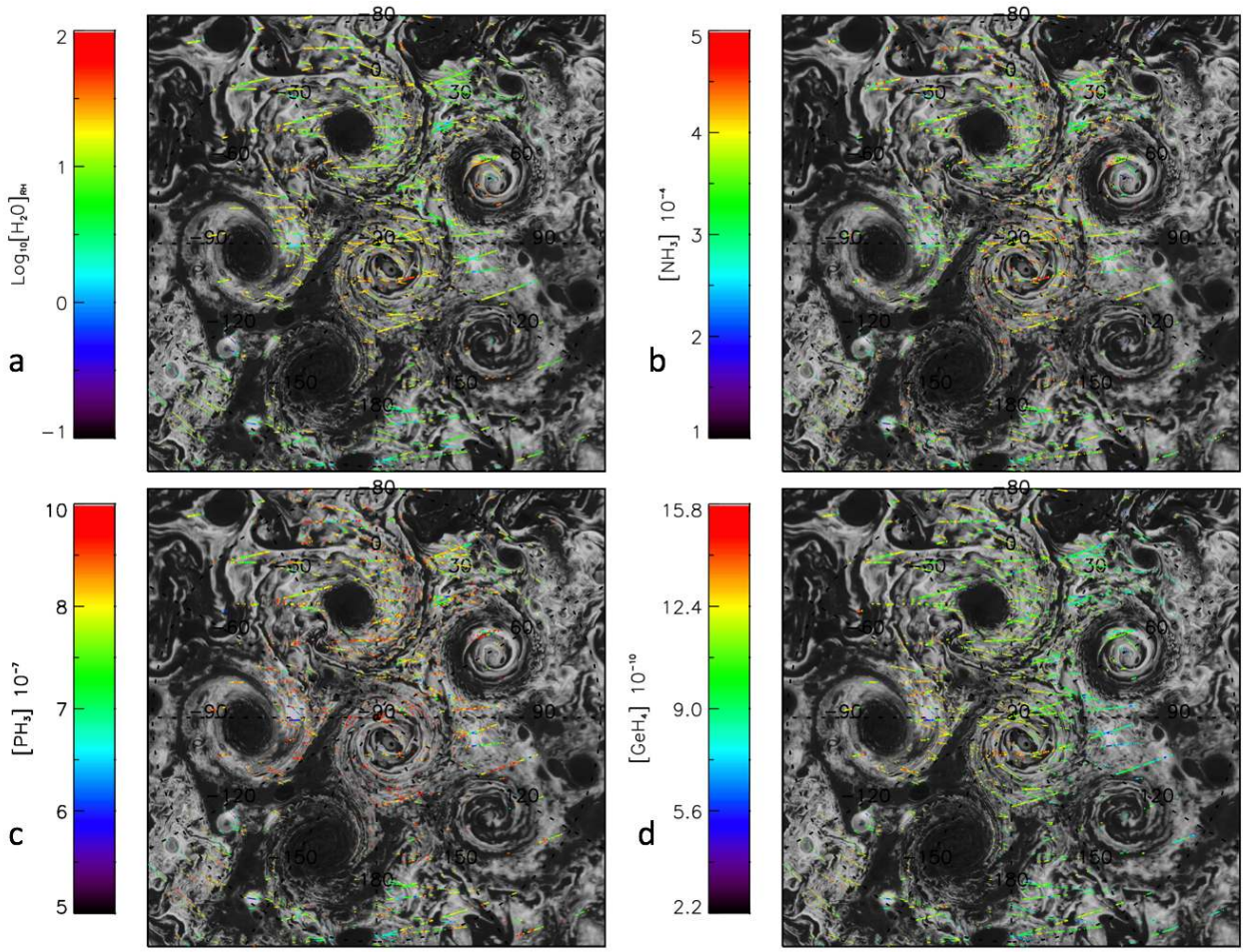


**Figure 9.** South pole maps of water relative humidity (a), ammonia (b), phosphine (c) and germane (d) concentrations.

Areas with the lowest cloud cover are found to be considerably depleted in disequilibrium species ($PH_3$ and $GeH_4$) once compared against moderately cloudy ones, suggesting effective suppression of vertical upwelling (see Figures 7 and 8). **$PH_3$ has abundances of the order of 0.6-1 ppm in the north while it reaches up to 2 ppm in the south. Also the $GeH_4$ shows the same difference between north and south with values of 6-10 ppb values that reach 15 ppb respectively. However, the comparison of absolute values between the two poles must also consider the effective better spatial resolution of the southern spectra for most of JIRAM data, capable therefore of singling out more extreme values.**

$PH_3$ and $GeH_4$ are not stable at the pressure and temperature conditions of the upper troposphere where they are detected. They are usually interpreted as tracers of active vertical motions that replenish the upper levels with fresh material from the much deeper atmosphere, where they are in equilibrium. The concentration contrasts between bright and dark area appear stronger over the northern pole and the depletion of germane looks stronger than for phosphine (see Figure **10). The ratio $[PH_3]/[GeH_4]$ is the order of a thousand.**

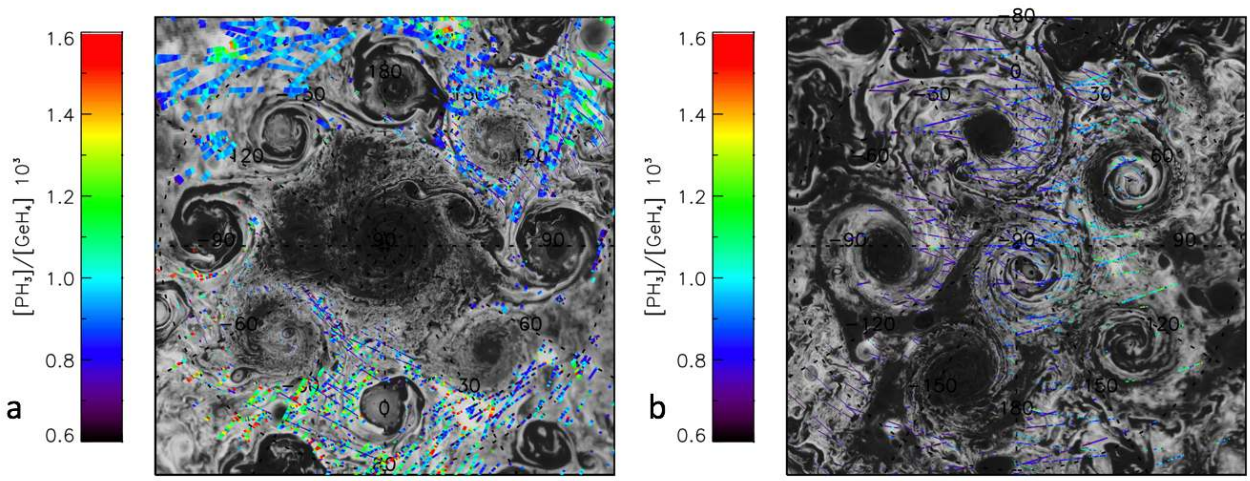


**Figure 10.** Maps of phosphine to germane ratio for the North (left panel) and for the South (right panel)

## 4. Dynamics

The process of mosaicking, as seen in Figures 1, 2 and 3, can alter the original images as a re-pixelization process is necessary to create maps. Because of the lowering of the orbit over North Pole, we achieved a resolution better than 16 km for some of the images during PJ9 pass. From a visual analysis of those images, the existence of wavy structures over some parts of the polar cyclones could be conjectured. In fact, a more sophisticated analysis by using 2D Fourier filtering to highlight short-wavelength (high-frequency) perturbation has been applied to some of the single images not affected by image processing. The analysis revealed the presence of many wavy structures hovering near some part of the cyclones. This topic is better described by Moriconi et al. (2019) but an example is given in Figure **11** where the upper panel shows one of the original images taken by JIRAM approaching the northern CPC#2. A 2D Fourier filtering applied to the image provides the result illustrated in the second panel where the full wavy structure has been isolated from the image background. The result indicates a strong dynamical interaction between the lower level, where presumably the top of the cyclones is, with the higher levels of the troposphere. The upper level waves appear to have a typical wavelength of about 20-30km. The wavy perturbations may be induced by the ascending currents in some areas of cyclones that perturb the atmosphere above the cyclones, or they could result from the interaction of the surface wind field with the vortex population, analogously to Langmuir turbulence in the upper turbulent layer of Earth's oceans, the so-called ocean mixed-layer (Hamlington et al., 2014).

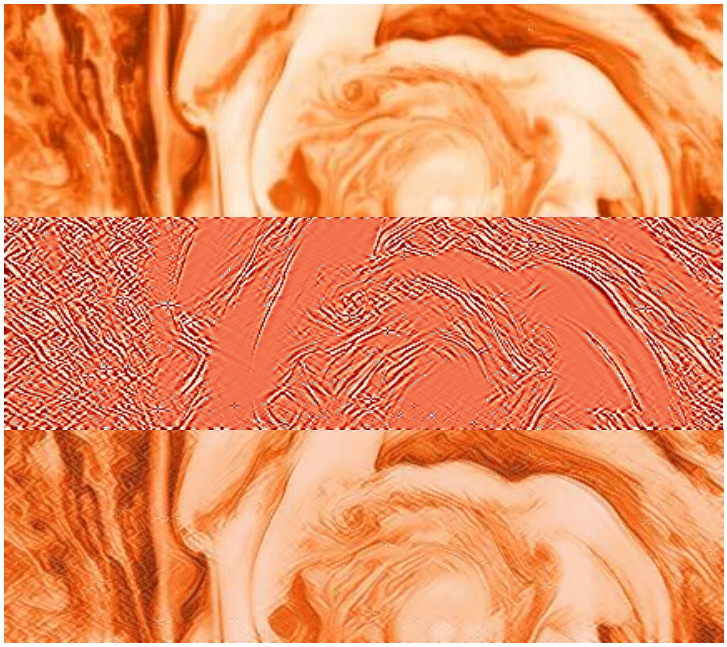

**Figure 11.** Waves over the cyclone #2 at the North Pole. Upper panel: original JIRAM image; central panel: result of the 2D Fourier high-pass filtering on the original image; lower panel: superimposition of the central panel to the upper panel.

A more in-depth analysis to understand the structure of the polar cyclones has been performed by attempting a comparative **power spectrum** investigation of long-living mesoscale (~100 km diameter) cyclones in Earth's ocean. In fact, the semi-stable, turbulent instabilities observed at Jupiter's Poles within and around the patterns of cyclones are reminiscent of the dynamics and instabilities observed in the buoyancy distributions in the Earth's oceanic mixed-layer (McWilliams, 2016) or in the potential temperature anomalies in the upper tropopause (Hakim et al. 2002). In the ocean, these instabilities develop at scales smaller than the local Rossby deformation radius, between few hundred meters and 2-3 km, and contribute to the internal structure of mesoscale vortices and to very large vertical velocities and intense vertical exchanges (e.g Zhong et al., 2017). They are associated **with** the development of fronts at scales where the planetary rotation is still important but not dominant, and are characterized by intense vertical velocities (McWilliams, 2016).

The emergence of these kilometer-scale fronts cannot **generally** be described by quasigeostrophic (QG) models, developed by Charney (1971) to describe in a conceptually simple, two-dimensional framework, the dynamics of atmospheric and oceanographic flows with horizontal length scales which are very large compared to their vertical extension whenever the strength of inertia is small compared to the strength of the Coriolis force. On the other hand, the laterally divergent flows associated with frontogenesis is approximated in two-dimensions **whenever the QG model is applied to a semi-infinite domain with zero potential vorticity (PV) in the interior. In this special case the so-called Surface Quasi-Geostrophy (SQG) approximation, first introduced by Blumen (1978) assumes that the flow evolution is controlled by the advection–diffusion of surface buoyancy at the boundary. It is based on the conservation of this active scalar (surface buoyancy) along the horizontal geostrophic flow, and links velocity and buoyancy.**

The SQG model has shown some success in interpreting turbulent dynamics in the troposphere (Held et al. 1995), the dominance of cyclones over anticyclones at the tropopause (Hakim et al. 2002), and more recently, observations in the oceanic mixed-layer (Lapyere and Klein, 2006).

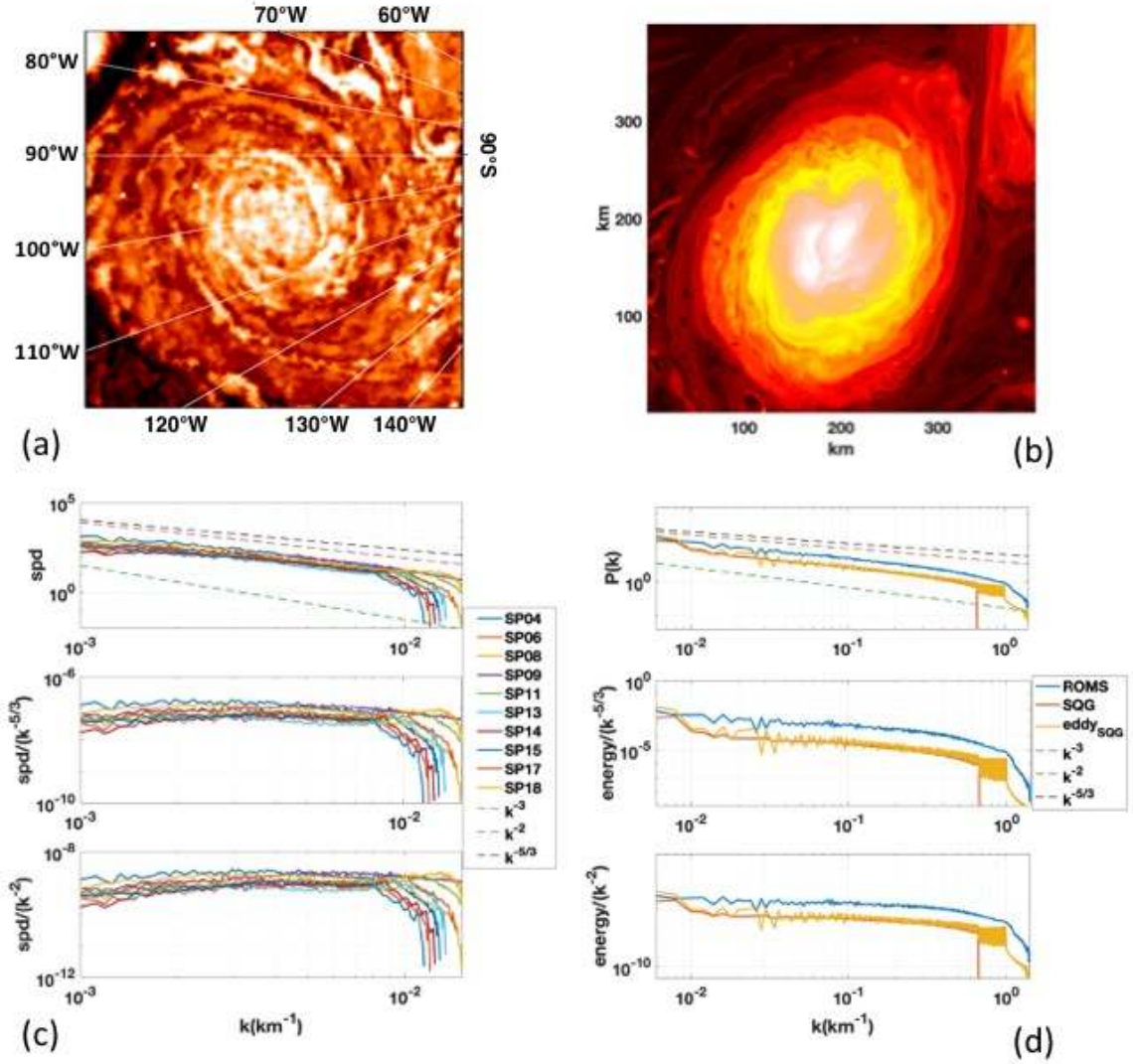


**Figure 12.** (a) Jupiter cyclone #4 from South Pole PJ4 image. (b) Cyclonic eddy in surface buoyancy in a freely-decaying SQG simulation at a resolution of 1024 x 1024. Several Gaussian shaped cyclones are seeded as initial conditions in a freely-decaying, unforced run. The figure shows one of the remaining cyclones after approximately 50 rotation periods. (c) 2D power spectra for selected data sets from Jupiter South Poles; the power spectra calculated for Jupiter are related to the latitudes higher than 82°S that are dominated by the presence of the polar cyclones. (d) 2D power spectra for the cyclone in panel (b) in light orange, for the whole SQG field at the time the cyclone was extracted in dark orange, and for an ocean cyclonic eddy obtained by ROMS run in the Gulf Stream region at horizontal resolution of 750 m (courtesy of J. Gula). The ocean cyclone is approximately 200 km in diameter and the non-dimensional SQG eddy has been scaled to match it.

One characteristic that sets apart SQG, and flows in the oceanic mixed-layer**,** from **"traditional"** QG **and two-dimensional** turbulent flows is the slope of the energy power spectra, which is shallower than the non-local $E(k) \propto k^{-3}$ predicted for two-dimensional and QG systems in the direct cascade range (e.g. **Bracco et al., 2004;** Bracco and McWilliams, 2010). An energy spectrum as steep or

steeper than $k^{-3}$ is indicative of non-local dynamics, where coherent, large scale vortices dominate. The theoretical SQG slope of buoyancy variance in the direct energy cascade range is indeed $\propto k^{-5/3}$, indicative of local dynamics, where frontal and filamentary structures at scales smaller than the large coherent vortices control mixing. These local dynamics are behind the large vertical velocities and their localization in circulations of scales smaller than the Rossby deformation radius of the flow. Numerical simulations in various configurations using both the SQG approximation, or the primitive equations commonly employed by ocean models, concur in finding spectral slope**s** slightly steeper than $k^{-5/3}$ and usually approaching $k^{-2}$ (Pierrhumbert et al., 1994**; Held et al., 1995**; Capet et al., 2008; Zhong and Bracco, 2013). The steepening of the theoretical slope is commonly found in presence of large vortices**, but could also be related to numerical diffusion**.

In Figure **12**, the power spectra calculated on the full two-dimensional image mosaics return slopes consistent with the SQG model. **The analysis here was done following the empirical correspondence between power spectra of atmospheric kinetic energy and those of cloud opacities as done by Harrington et al. (1996) for Jupiter on the basis of Travis (1978) previous results on Venus and Earth. Travis, in fact, found a close correspondence between power spectra of atmospheric kinetic energy and power spectra of visible and infrared cloud intensities.** The same figure shows an eddy obtained integrating the SQG equation using a pseudo-spectral code and resolution 1024 x 1024 grid points over a $2\pi$ x $2\pi$ non-dimensional domain; the eddy occupies nearly 1/4 of the model domain. The cyclone's energy spectra are shown with the whole domain one **that includes two more cyclones eddies,** and the spectrum of an upper ocean cyclone simulated by the Regional Ocean Modeling System (ROMS, Shchepetkin and McWilliams, 2005) at 750 m horizontal resolution (Gula et al., 2015).

**The energy power spectra consistency is supported by a visual similarity, but other turbulent systems are characterized by analogous slopes. For example, a recent work (Novi et al. 2019) has shown that rapidly rotating convective flows can generate intense vortices close to the Poles on a spherical planet in local Cartesian approximations. These convective flows also have slopes close to $k^{-2}$ but the structure of convective plumes and their vertical velocities appear to be more disorganized within the eddy (see, for a convective cyclonic plume in the high latitude Earth's ocean, Fig. 4 in Sun et al., 2017).**

## 5. Conclusions

Differences between Jupiter's North Pole and South Pole are evident not only by counting the number of persistent cyclonic structures or the anticyclonic activity but also by other properties such as cloudiness, size, and concentration of minor and trace atmospheric species such as water vapor, ammonia, phosphine and germane. The question is whether these differences are only the consequence of an evolution of the two polar zones that proceeds on different time scales or, instead, there is a persistent and more profound connection with the deepest part of the Jovian atmosphere, such as its magnetic field which results to have a very different structures between north and south. In relation to the stability of the vortex configurations found at Jupiter's poles, Reinaud (2019) recently investigated the conditions under which an array of *m* three-dimensional, unit Burger number, quasi-geostrophic vortices on a ring, with an additional vortex lying on the array center, are in mutual equilibrium. He found that the central vortex, if moderate in strength and having the same rotation sign of the peripheral ones, stabilizes the vortex array for a long time in a QG system. He

refers specifically to the cluster of cyclones of Jupiter's polar regions as an example of environmental context where his study can be applied. On the other hand, our comparative analysis shows similar results for cyclones in both the Jupiter and the Earth's case cyclone in the upper ocean mixed-layer, with the size of the cyclones being proportional to the size of the planet to which they belong to. It also suggests the possibility of a well-mixed upper boundary layer on Jupiter's Poles with the cyclones being key mediators of any exchange with deeper layer(s) though large vertical velocities localized in frontal regions that result from local, non-geostrophic dynamics. Indications of the possible presence of fronts come from the strong gradients in optical depth and small scale structure in and around the cyclones. Finally, although our work on JIRAM data has provided insights into the dynamics of Jupiter's polar regions, additional measurements from Juno's other instruments, like the Juno's MicroWave Radiomenter (MWR) which is able to sound deeper in the atmosphere, and corresponding analyses are necessary to explain the origin of Jupiter's curious polar cyclones.

**Acknowledgements**

This work was supported by the Italian Space Agency through ASI-INAF contract I/010/10/0 and 2014-050-R.0. Orton was supported by NASA with funds distributed to the Jet Propulsion Laboratory, California Institute of Technology.

The JIRAM instrument was developed by Leonardo at the Officine Galileo - Campi Bisenzio site.

**The data used for this study will be available once the proprietary period ends from the NASA's Planetary Data System at https://pds.jpl.nasa.gov/tools/data-search/.**

**References**

Acton, C.H. (1996). Ancillary data services of NASA's Navigation and Ancillary Information Facility *Planetary and Space Science*, **44**, 65-70, doi: 10.1016/0032-0633(95)00107-7

Adriani, A., **et al. (2016) Juno's Earth flyby: the Jovian infrared Auroral Mapper preliminary results. Astrophysics and Space Science, 361 (8), article id.272.**

**Adriani, A.,** Mura, A., Orton, G., Hansen, C., Altieri, F., Moriconi, M.L., Rogers, J., Eichstädt, G. et al. (2018). Clusters of Cyclones Encircling Jupiter's Poles. *Nature*, **555**, 216-219, doi: 10.1038/nature25491

Adriani, A., Filacchione, G., Di Iorio, T., Turrini, D., Noschese, R., Cicchetti, A., Grassi, D., Mura, A., et al. (2017). JIRAM, the Jovian Infrared Auroral Mapper. Space Science Reviews, 213, 393-446, doi: 10.1007/s11214-014-0094-y

Blumen, W. (1978). Uniform potential vorticity flow: Part I. Theory of wave interactions and two-dimensional turbulence. *Journal of Atmospheric Science*, **35**, 774–783.

Bolton, S.J., Lunine, J.I., Stevenson, D., Connerney, J.E.P., Levin, S., Owen, T. C., Bagenal, F., Gautier D., et al. (2018). The Juno Mission. *Space Science Reviews*, **213**, 5-37, doi: 10.1007/s11214-017-0429-6.

Bracco, A. & McWilliams, J.C. (2010). Reynolds-number dependency in homogeneous, stationary two-dimensional turbulence. *Journal of Fluid Mechanics*, **646**, 517-526.

**Bracco A., J von Hardenberg, A. Provenzale, J. Weiss & J.C. McWilliams (2004). Dispersion and mixing in quasigeostrophic turbulence, *Physical Review Letters*, 92, 084501-1 - 4**

Capet X., Klein P., Hua B.L. Lapeyre, G., & McWilliams J.C., (2008), Surface kinetic and potential energy transfer in SQG dynamics. *Journal of Fluid Mechanics*, **604**, 165–174.

Charney, J.G. (1971). Geostrophic turbulence. *Journal of Atmospheric Science*, **28**, 1087–1095, doi: 10.1175/1520-0469(1971)028<1087:GT>2.0.CO;2

**Drossart, P., et al. (1998) The solar reflected component in Jupiter's 5-µm spectra from NIMS/Galileo observations, J. Geophys. Res., 103 (E10), doi:10.1029/98JE01899**

Giles, R.S., Fletcher, L.N., & Irwin P.G.J. (2015). Cloud structure and composition of Jupiter's troposphere from 5-m Cassini VIMS spectroscopy, *Icarus*, **257**, 457-470, doi:10.1016/j.icarus.2015.05.030.

Giles, R.S., Fletcher, L.N., & Irwin P.G.J. (2017). Latitudinal variability in Jupiter's tropospheric disequilibrium species: GeH4, AsH3 and PH3, *Icarus*, **289**, 254-269, doi:10.1016/j.icarus.2016.10.023.

Grassi, D., Adriani, A., Mura, A., Dinelli, B.M., Sindoni G., Turrini D., Filacchione, G., Migliorini, A., et al (2017a). Preliminary results on the composition of Jupiter's troposphere in hot spot regions from the JIRAM/Juno instrument. *Geophysical Research Letters*, **44** (10), 4615-4624, doi:10.1002/2017GL072841.

Grassi, D., Ignatiev, N.I., Sindoni, G., D'Aversa E., Maestri T., Adriani, A., Mura, A., Filacchione, G., et al (2017b). Analysis of IR-bright regions of Jupiter in JIRAM-Juno data: Methods and validation of algorithms. *Journal of Quantitative Spectroscopy and Radiative Transfer*, **202**, 200-209, doi:10.1016/j.jqsrt.2017.08.008.

Gula, J., Molemaker M.J. & McWilliams, J.C. (2015). Gulf Stream dynamics along the southeastern U.S. Seaboard. *Journal of Physical Oceanography*, **45**, 690–715, doi:10.1175/JPO-D-14-0154.1.

Irwin, P.G.J., Weir, A.L., Smith, S.E., Taylor, F.W., Lambert, A.L., Calcutt, S.B., Cameron- Smith, P.J., Carlson R.W., et al. (1998). Cloud structure and atmospheric composition of Jupiter retrieved from Galileo near infrared mapping spectrometer real-time spectra. *Journal of Geophysal Research Planets*, **103** (E10), 23001-23021, doi:10.1029/98JE00948.

Hakim G.J., Snyder C. and Muraki D. J. (2002), A new surface model for cyclone–anticyclone asymmetry. *J. Atmos. Sci*., **59**, 2405–2420.

Hamlington P.E., Van Roekel P., Fox-Kemper B. et al. (2014), Langmuir–Submesoscale Interactions: Descriptive Analysis of Multiscale Frontal Spindown Simulations. J. Physic. Ocean., **44**, 2249-2272, doi:10.1175/JPO-D-13-0139.1.

**Hansen, C.J. et al. (2014). Junocam: Juno's Outreach Camera, Space Sci. Rev. doi 10.1007/s11214-014-0079-x.**

**Harrington J., T.E. Dowling, and R.L. Baron (1996). Jupiter Tropospheric Thermal Emission: II. Power Spectrum Analysis and Wave Search. Icarus, 124, 32-44, doi: 10.1006/icar.1996.0188**

Held I.M., Pierrehumbert R.T., Garner S.T., et al (1995), Surface quasi-geostrophic dynamics. J. *Fluid Mech.* **282**, 1–20.

Lapeyre G. and Klein P. (2006), Dynamics of the upper oceanic layers in terms of surface quasigeostrophy theory. *J. Phys. Oceanogr*., **36**, 165–176.

McWilliams JC. (2016), Submesoscale currents in the ocean. *Proc. R. Soc. A* **472**: 20160117, http://dx.doi.org/10.1098/rspa.2016.0117

561 Moriconi M.L., A. Migliorini, F. Altieri, et al. (2019), Power spectrum analysis of Jupiter's polar
562 clouds by Juno/JIRAM data, submitted to *JGR* Planets.

563 Pierrehumbert, R.T., I.M. Held and K.L. Swanson (1994) Spectra of local and nonlocal two-
564 dimensional turbulence. *Chaos, Solitons, Fractals* **4**, 1111–1116.

565 Reinaud J.N. (2019), Three-dimensional quasi-geostrophic vortex equilibria with m-fold symmetry,
566 J. Fluid Mech., **863**, 32_59, Cambridge University Press 2019, doi:10.1017/jfm.2018.989

567 **Seiff, A. et al. (1998) Thermal structure of Jupiter's atmosphere near the edge of a 5-µm hot**
568 **spot in the north equatorial belt, J. Geophys. Res., 103 (E10), doi:10.1029/98JE01766.**
569 **Available as** numerical data as GP-J-ASI-3-ENTRY-V1.0, NASA Planetary Data System.

570 Shchepetkin A.F., and J.C McWilliams JC. (2005), The regional oceanic modeling system: a split-
571 explicit, free-surface, topography-following coordinate oceanic model. *Ocean Model* **9**,
572 347–404. doi: 10.1016/j.ocemod.2004.08.002

573 **Sun, D., T. Ito, & A. Bracco (2017) Oceanic uptake of oxygen during deep convection events**
574 **through diffusive and bubble mediated gas exchange *Global Biogeochem. Cycles*, 31,**
575 **https://doi.org/10/1002/2017GB005716**

576 **Travis L.D. (1978). Nature of atmospheric dynamics on Venus from power spectrum analysis**
577 **of Mariner 10 images. J. Atmos. Sci., 35, 1584-1595, doi: 10.1175/1520-**
578 **0469(1978)035<1584:NOTADO>2.0.CO;2**

579 Zhong, Y., A. Bracco, J. Tian, J. Dong, W., Zhao, Z. Zhang (2017), Observed and simulated
580 vertical pump of an anticyclonic eddy in the South China Sea. Scientific Report , 44011,
581 doi:10.1038/srep44011

582 Zhong Y., and A. Bracco (2013), Submesoscale impacts on horizontal and vertical transport in the
583 Gulf of Mexico, *J. Geoph. Res. - Oceans*, **118**, 5651-5668, doi:10.1002/jgrc.20402

584